Thermal Metrology of Silicon Microstructures Using Raman Spectroscopy

Mark R. Abel, Tanya L. Wright, William P. King, and Samuel Graham

***Abstract*—Thermal metrology of an electrically active silicon heated atomic force microscope cantilever and doped polysilicon microbeams was performed using Raman spectroscopy. The temperature dependence of the Stokes Raman peak location and the Stokes to anti-Stokes intensity ratio calibrated the measurements, and it was possible to assess both temperature and thermal stress behavior with resolution near 1 μm. The devices can exceed 400 °C with the required power depending upon thermal boundary conditions. Comparing the Stokes shift method to the intensity ratio technique, non-negligible errors in devices with mechanically fixed boundary conditions compared to freely standing structures arise due to thermally induced stress. Experimental values were compared with a finite element model, and were within 9% of the thermal response and 5% of the electrical response across the entire range measured.**

***Index Terms*—Heated atomic force microscope (AFM) cantilever, microscale thermometry, Raman spectroscopy, thermal microelectromechanical systems (MEMS).**

I. Introduction

A. Motivation

THE design and characterization of microelectronics and microelectromechanical systems (MEMS) devices has placed increased demands upon advances in thermal metrology. This has been especially true for MEMS systems where function and reliability depend on temperature control. Examples of such devices include microthermal actuators [1]–[3], semiconductor gas sensors utilizing polysilicon microhot plates [4], [5], micropolymerase chain reaction (PCR) well arrays [6]–[8], micropower generation sources [9], [10], and heated atomic force microscope (AFM) cantilevers for data storage [11], [12]. With the exception of microPCR arrays, these thermal devices can exceed temperatures of 300 °C and often contain critical features on the order of 10 μ m or less. Therefore, thermal measurement techniques are needed which have high spatial and temperature resolution over a broad range of temperatures; these requirements make thermal metrology at this level very challenging.

In general, temperature measurements in microdevices can be performed using either optical or electrical temperature sensors. Optical methods are the most desirable as they are inherently non-contacting and do not interfere with the performance of kinetic devices and have the potential for full-field mapping with high spatial resolution. However, these measurements are not trivial. Techniques such as microinfrared thermography (micro-IR) can provide a temperature resolution less than 1 °C and spatial resolution of 5 μm when using far-field diffraction-limited optics. At this spatial resolution, details of the temperature distribution in MEMS devices can be lost. For MEMS devices that operate over a large temperature range, the difficulty of calibrating surface emissivity of thin-film structures can reduce confidence in temperature readings.

Methods such as laser thermoreflectance have been used for both submicron and gigahertz monitoring of surface temperature changes [13]–[16]. In thermoreflectance, changes in the temperature of a sample result in small deviations in optical reflectivity. The magnitude of the deviation depends upon the temperature dependence of the optical constants (refractive index and extinction coefficient). In order to maximize thermoreflectance signals, coatings are often used in combination with cyclic heating and lock-in detection. Temperature resolutions of 10 mK have been achieved [17], however, the calibrations are limited to relative temperature changes [18]. Other examples of optical thermometry include Raman imaging, fluorescence thermometry, and interferometry as reviewed in [19].

Raman spectroscopy is well suited for the temperature measurements in MEMS devices, especially silicon MEMS due to the strong scattering cross section of silicon. When using a visible light source, Raman spectroscopy can provide spatial resolutions on the order of 1 μm or less, using far field diffraction limited optics. Due to the relatively long photon collection times, this technique is generally applied in steady state measurements. Raman scattering has been used to determine the temperature distribution with micron spatial resolution in diamond structures [20], silicon electronics [21]–[23], III-V semiconductors [24]–[27], and polysilicon MEMS [28]. In spite of the power of this technique, it has received very little attention in the application to thermal MEMS devices. Additional research is needed to validate its accuracy and applicability, and explore the limitations of this technique as a thermal metrology tool for MEMS.

Manuscript received July 18, 2005; revised November 22, 2005. This work was supported by Sandia National Laboratories under the Laboratory Directed Research and Development (LDRD) Program and the United States Department of Energy's National Nuclear Security Administration under Contract DE-AC04-94AL85000. This work was recommended for publication by Associate Editor J. Parry upon evaluation of the reviewers comments.

M. R. Abel was with The George W. Woodruff School of Mechanical Engineering, Georgia Institute of Technology, Atlanta, GA 30332 USA. He is now with Intel Assembly Technology Development, Chandler, AZ 85226 USA (e-mail: mark.r.abel@intel.com).

T. L. Wright was with the The George W. Woodruff School of Mechanical Engineering, Georgia Institute of Technology, Atlanta, GA 30332 USA. She is now with the Schlumberger Riboud Product Center, Clamart 92140, France (e-mail: twright@clamart.oilfietd.slb.com).

W. P. King and S. Graham are with the The George W. Woodruff School of Mechanical Engineering, Georgia Institute of Technology, Atlanta, GA 30332 USA (e-mail: william.king@me.gatech.edu; sgraham@me.gatech.edu).

Color versions of one or more of the figures in this paper are available online at http://ieeexplore.ieee.org.

Digital Object Identifier 10.1109/TCAPT.2007.897993

B. Raman Spectroscopy

The Raman Effect is manifested through the inelastic scattering of a small portion of photons (1 in 10^7) which exchange energy with the phonon vibrations in a crystal lattice. The inelastic scattering results in a frequency shift of the scattered photon to longer wavelengths (Stokes shift) or shorter wavelengths (Anti-Stokes shift) [19]. The (angular) frequency of the scattered photon is given by $\omega_s = \omega_i \pm \omega_l$ where ω_i is the frequency of the incident photon, ω_l is the frequency of the lattice vibration, and ω_s is the frequency of the scattered photon. The temperature dependence of this frequency shift arises from the anharmonicity of the interatomic potentials. Thus, changes in ω_l can occur as a result of the contraction or expansion of the crystal lattice upon thermal and structural loadings. It is possible to obtain the temperature from the Raman spectra through the ratio of the Stokes to anti-Stokes intensities, by the magnitude of the Raman Stokes frequency shift, or changes in the linewidth of the Stokes signal. The temperature dependent ratio of the Stokes to anti-Stokes peaks is given by [19]

$$\frac{I_{\text{Stokes}}}{I_{\text{Anti-Stokes}}} = \left(\frac{\omega_i - \omega_l}{\omega_i + \omega_l}\right)^4 \exp\left(\frac{\hbar\omega_l}{kT}\right) \tag{1}$$

where $\hbar$ is Planck's constant divided by 2π, k is the Boltzmann constant, and T is the absolute temperature. This equation is dependant on the temperature, scattering cross-section, and absorptivity (not shown) of the material of interest [29]. It should be noted that the Stokes shift is a result of energy being added to the material lattice and the anti-Stokes due to energy being removed. The ratio of these two Raman intensities are related to the availability of phonon states which is governed by the Bose–Einstein distribution and is a sole function of temperature. As the temperature increases in a non-metallic solid, this ratio tends towards unity. Temperature measurements using the intensity ratio method at high temperatures can become challenging as small changes in this ratio will result in large changes in temperature prediction. Greater precision in determining temperature over a broad range of temperatures may be obtained by modeling the absolute frequency shift using the following [20]:

$$\omega_{\text{shift}} = \omega_0 + A\left(1 + \frac{2}{e^{\frac{\hbar\omega_o}{2kT}} - 1}\right) + B\left(1 + \frac{3}{e^{\frac{\hbar\omega_o}{3kT}} - 1} + \frac{3}{\left(e^{\frac{\hbar\omega_o}{3kT}} - 1\right)^2}\right) \tag{2}$$

where A, B, and ω_0 are material specific parameters. The linewidth of the first silicon phonon resonance may be modeled with an equation of the same form as (2) [29]. This increase in linewidth occurs with increasing temperature due to increased optical phonon relaxation rates.

Following (1), the ratio of the Stokes to anti-Stokes intensities is indifferent to stresses which can arise in many thermal MEMS structures. Collection times and instrument calibration for measuring both the anti-Stokes and Stokes response can be long due to the relatively weak response of the anti-Stokes signal. On the other hand, the Stokes response provides a much stronger signal; up to an order of magnitude greater than the anti-Stokes response. Thus, monitoring the Stokes peak will yield much faster times for mapping temperature. However, the Stokes peak position is also affected by stresses which may evolve in a MEMS structure, causing error in the thermometry. Attempts to measure temperature by using simply the Stokes response for MEMS is especially attractive as it provides an easy method for calibrating absolute temperature. Although (2) is a non-linear relationship over a much larger temperature range, the authors have approximated a linear response of the Stokes peak position for silicon between room temperature and 1000 °C, which is sufficient for most thermal MEMS. A linear dependence of the Stokes shift with stress was also found between −300 and 300 MPa [30]. In this work, an analysis which compares these two measurement techniques on the same device is presented; one that has not been seen in previous studies. This analysis is intended to provide an in depth analysis for this metrology technique, and show importance of residual stresses in temperature measurements and the viability of using only the Stokes shift measurement technique.

II. Experimental

A. Sample Preparation

In this study, both electrically heated microbeams and heated AFM cantilevers were tested. These devices where chosen due to their wide range of use in developing a number of sensors, actuators, and scanning probe microscopy techniques. The microbeams also presented different boundary conditions from the AFM cantilever. The AFM cantilever was fully released from the underlying substrate and was expected to encounter very low thermal stresses during operation. The microbeams were fixed between two silicon anchor pads and either attached or released from an underlying oxide layer. Both configurations induce displacement constraints on the expanding microbeam which induces varying levels of thermal stresses.

The heated AFM cantilevers were fabricated using conventional IC manufacturing, and the details are described elsewhere [31]. The legs of the cantilever are Phosphorus doped to 2×10^{20} cm^{-3}, and the region that connects the two legs and supports the actual AFM tip is Phosphorus doped to 5×10^{17} cm^{-3}. Fig. 1 shows predictions for the temperature-dependence of the electrical resistivity of the two regions of doped silicon. The lower concentration of dopant atoms in the heater region gives it a higher resistance and the ability to effectively heat itself only in that localized region, with relatively small power dissipation. Fig. 2 shows the heated AFM cantilever used in this study.

To fabricate the microbeam heaters, 2.2-μm polysilicon films were grown using low pressure chemical vapor deposition (LPCVD) on 4 μm of silicon dioxide. The silicon dioxide layers were grown by plasma enhanced chemical vapor deposition (PECVD) on 100-mm single crystal silicon substrates. The polysilicon films were Phosphorous doped using ion implantation. Following the implantation, the dopant atoms were uniformly distributed throughout the polysilicon by depositing a thin oxide on the surface, annealing at 1100 °C for 1 h, and removing the cap oxide with hydrofluoric (HF) acid. This process yielded a theoretical uniform concentration of 2×10^{20} cm^{-3}as modeled by SSUPREM3 Software. Following this anneal, photolithography was used to mask and etch straight beams connected to 1 mm × 1 mm polysilicon pads. A second mask was used to deposit metal contacts on the

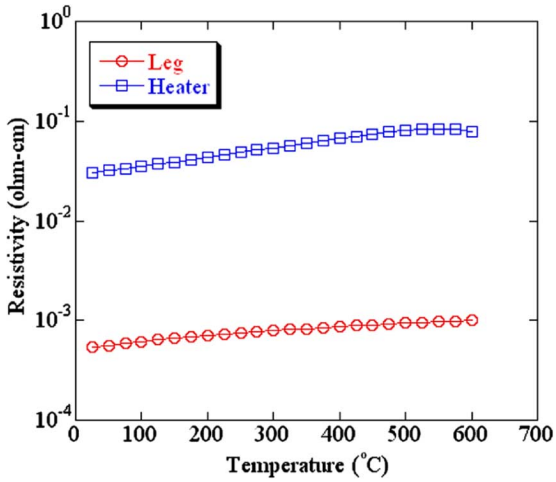

Fig. 1. Predictions of temperature dependant electric resistivity of heater and leg regions of AFM cantilever.

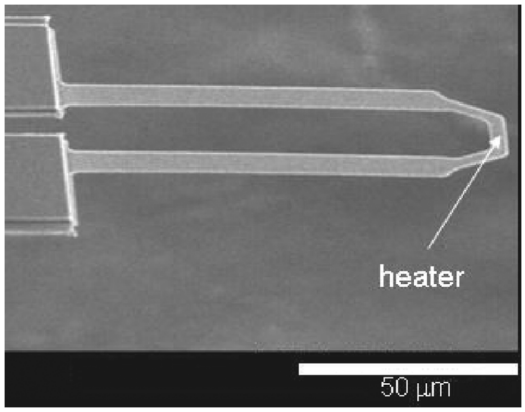

Fig. 2. SEM image of an electrically heated AFM cantilever. The cantilever heater is isolated at the end of the cantilever in the low doping region.

polysilicon pads, which made bonding to electrical connections possible. The wafers were then diced to make use of each device separately.

Sample 1A consisted of a straight beam (dimensions: 10 μm $\times$ 300 μm, Fig. 3) that was not released from the oxide. This resulted in a large residual tensile stress in the polysilicon layer which is expected to vary with the heating of the beam. This structure is typical of multilayer devices fabricated on low thermal conductivity layers such as found in microhotplates. Sample 1B was a straight beam as shown in Fig. 3, but released from the substrate by masking the aluminum pads, and etching in diluted HF acid. This released structure ranged from being nearly stress free to having residual tensile stresses, depending on the etch time. These two configurations (released and unreleased) also provided important thermal boundary conditions for the performance of these thermal MEMS since the mode of heat dissipation is primarily through conduction and radiation. The thermal conductivity of the silicon dioxide is greater than that of air by over an order of magnitude. Thus, by removing the oxide under the beam, the heat sink it provides is no longer present, and the beam reaches greater temperatures with the same power dissipation.

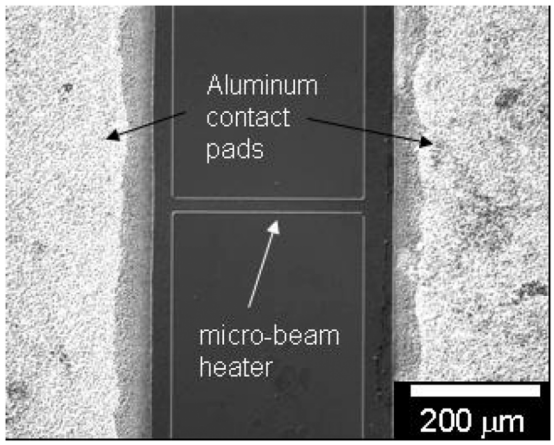

Fig. 3. Polysilicon microbeam heater on oxide, sample 1A. (Sample 1B similar).

B. Measurements

A Renishaw InVia Raman Microscope with 180° backscattering geometry was used to measure all devices in this study. The spectrometer has a focal length of 250 mm, and a diffraction grating with 3000 lines/mm in minus one order, yielding a spectral dispersion of 0.507 cm^{-1}/charge coupled device (CCD) pixel when a slit width of 15 μm is utilized. Because the minimal linewidth of silicon is 3.5–4.0 cm^{-1} at room temperature, this resolution is sufficient to detecting peak shifts within $\pm$ 0.1 cm^{-1} using peak fitting software. A 488 nm laser line was used for sample excitation, and was set to a sample power 45.4 μW as measured by a Newport optical power meter. This power setting insured there was no Stokes peak shift due solely to laser heating. A 50X objective with a numerical aperture (NA) of 0.75 was used collect the Raman signature of the devices. The laser spot size as measured by the CCD camera was estimated at roughly 800 nm by the instrument manufacturer. To calibrate the temperature measurements, Raman Stokes and anti-Stokes spectra were taken for a silicon sample between room temperature and 1000 °C using the method described in [30]. A single crystal silicon sample was heated in a controlled environmental stage (Linkham THMS 1500) to 1000 °C and the Raman spectrum measured. For the ratio intensity measurements, four minute scans of the Stokes and anti-Stokes peaks were taken every 100 °C. This long scan time was to insure an adequate signal to noise ratio (SNR) for the weak anti-Stokes resonance. The measurements were repeated ten times at each measurement in order to analyze the uncertainty in each measurement range. For the Stokes peak shift measurements, collection times were reduced to 45 s due to the strong Raman scattering response. Thermal stress was not expected to play a role in this calibration since the material was free to expand in all directions.

For the AFM cantilevers, Raman thermometry was performed at four points of interest along the structure: the heater center (1), heater corner (2), heater/leg transition (3), and leg front (4, see Fig. 4). These points gave insight to the temperature distribution from the heater region to the leg transition, which is the region of main interest, as the performance of this region determines its functionality. Only the heater center measured using both the

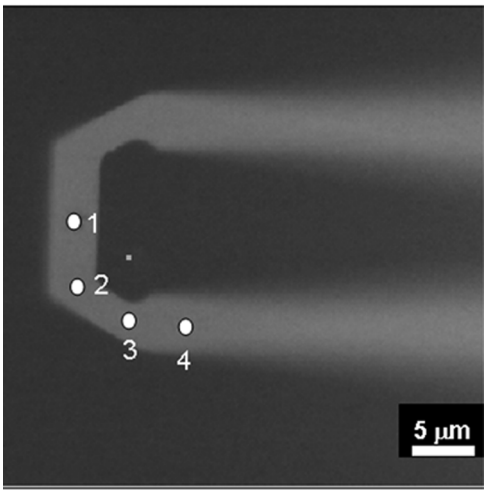

Fig. 4. Top view of AFM cantilever showing locations in and near the heater region probed with Raman spectroscopy.

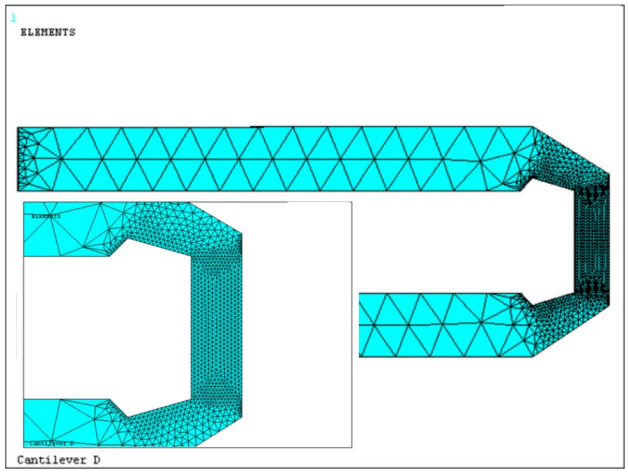

Fig. 5. FE mesh for the entire AFM cantilever and for the heater region (inset).

Stokes peak location and the intensity ratio methods. All other points were measured with only the Stokes resonance.

To power the cantilever and microheater devices, sense resistances of approximately 10 kΩ and 100 Ω, respectively, were placed in series with the devices and connected to a Keithley 2400 source meter. The dc power source was incremented in 1 V steps during measurements. To avoid a thermal runaway effect, the devices were operated up to a maximum voltage as determined by a resistance-voltage characterization prior to thermal testing. For the AFM cantilevers, the last five data points taken were in 0.5 V steps as the resistance versus voltage changes rapidly in this regime. The sense resistor helped to improve the sensitivity of the voltage measurements across the devices and was used to calculate the power dissipation in the structures. For spatial mapping of temperature, an automated Pryor XYZ translation stage with 0.1 μm in-plane resolution was used to position the devices under the Raman objective.

C. Finite Element Analysis

In order to compare theoretical calculations with experimental data, the finite element analysis (FEA) package of ANSYS Classic v7.1 was used to model the doped silicon structures. Thermal-electric multi-physics elements were used so that an input voltage could be applied to the geometry, and the resultant temperature distribution found. Temperature dependant thermal conductivity was supplied as a look-up table in ANSYS based upon data for doped silicon and air taken from the literature [32], [33]. The data for silicon from these references were modeled using a Boltzmann phonon transport model with relaxation time approximation in order to predict their thermal behavior at higher temperatures. The thermal conductivity of the PECVD silicon dioxide was measured using a modified $3-\omega$ experiment [34]. Electrical resistivity was modeled in Matlab as a function of doping level and temperature, and the resulting values were also used as an input for the FEA model (Fig. 5). To model the temperature dependent electrical resistivity, the following form was used:

$$\rho(T) = \frac{1}{q\mu(T)N(T)} \tag{3}$$

where q is the electron charge, $\mu(T)$ is the mobility, $N(T)$ is the number of extrinsic carriers and T is the temperature. Calculations for the temperature dependent mobility for phosphorus doped polysilicon were performed as presented in [35]. The heated AFM cantilever thickness of 600 nm was modeled as 10 separate volumes of 60 nm each in the heater section. Using the doping data from the SSUPREM3 model, the temperature dependant resistivity was averaged for each 60 nm volume, to account for the variable doping. Since the microbeams were uniformly doped, this averaging scheme was not necessary for their FEA analysis.

Both the thermal conductivity and electrical resistivity were modeled from room temperature to 600 °C, the expected maximum temperature of the devices. Heat loss from the surface to the ambient due to radiation was applied as a boundary condition to all surfaces of the heated structure, with an emissivity of 0.8 assumed for the silicon. This value was based on micro-IR experimentation and assumed constant over the experimental temperature range. While heat loss by natural convection is negligible for microdevices of these dimensions, due to the small Rayleigh numbers [36], heat loss by conduction into the surrounding air was found to be a significant mode of heat transfer. For this reason, a mesh was created surrounding AFM and microbeam devices, and given the properties of air to correctly model the heat loss to the ambient. Since the AFM device is a suspended structure with no substrate beneath surface radiative losses to a substrate were not necessary. For the microbeams, however, either conduction through the oxide layer to the silicon substrate (sample 1A) or direct radiation to the silicon substrate (sample 1B) was included. The model assumed a constant temperature over the cross-sectional areas at the both ends of the device. It is between these two surfaces where the voltage drop was applied. A fine mesh was used in the heater region (Fig. 5) in order resolve larger temperature gradients in the area of interest, while a much courser mesh was used in the leg regions.

The model was run for the same input voltage drops to the cantilever that was measured in the Raman experimentation. The experimental and model electrical response were compared to ensure there were matching power dissipations between the two.

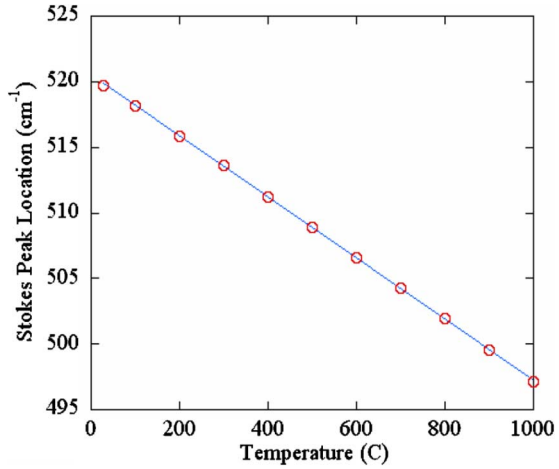

Fig. 6. Stokes peak frequency as a function of temperature for single crystal silicon. Data were approximated with a linear shift of the Stokes peak between room temperature and 1000 °C.

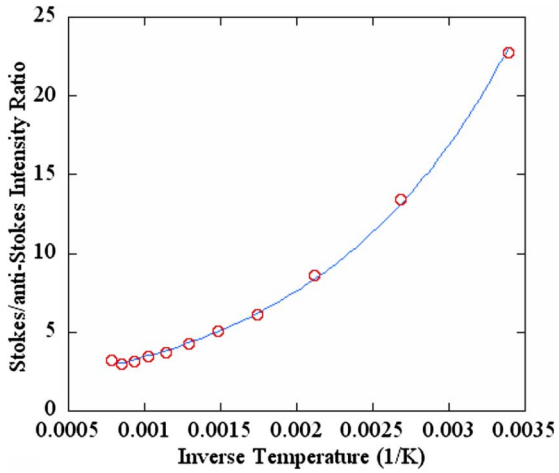

Fig. 7. Stokes/anti-Stokes intensity ratio as function of inverse temperature for single crystal silicon. Data show a nonlinear response with highest sensitivity at lower temperatures.

III. Results and Discussion

A. Calibration Results

The calibration of the Stokes shift with temperature is shown in Fig. 6. A linear relationship to the temperature dependence of the phonon frequency was found to be a very good approximation across the entire tested range (-0.0232 cm^{-1}/°C). A second calibration as a function of stress was determined using a millimeter scale four point bend specimen. The Stokes shift was also found to be a linear function of stress (-2.859 cm^{-1}/GPa). The calibration of the Stokes/anti-Stokes intensity ratio is shown in Fig. 7, also from room temperature to 1000 °C. By plotting the inverse temperature against the intensity ratio, an exponential decay was found, as expected from (1). Both calibrations yielded a correlation coefficient of greater than 0.99 using their respective fits.

The major contributions to the measurement uncertainty are from fitting the Stokes and anti-Stokes spectra along with determining the reference peak location at room temperature which is used to determine the relative Stokes shift. Other sources of uncertainty such as the uncertainty of curve fit parameters generally yield smaller contributions to the overall uncertainty [37]. The temperature uncertainty due to the Stokes reference peak location was found to be ±9 °C (bias error). To determine the uncertainty of the fitted peak location and peak intensity (precision errors), the mean and standard deviation was found for each temperature increment for a total of 10 measurements. Assuming a normal distribution, 95% of the scans will be within two standard deviations from the mean of each measurement. For the Stokes peak location, this deviation in wavenumbers from the mean peak location was found and converted to an equivalent temperature, as shown in Table I, which provides the uncertainty for a single measurement. The values in Table I for the intensity ratio method are taken as the overall uncertainty. For the Stokes peak location method, the uncertainties in Table I can be vector summed with the bias error of ±9 °C to determine the overall uncertainty. From room temperature to 700 °C, the maximum total uncertainty of the Stokes peak location is ±105 °C for a single measurement. For the Intensity ratio, the error is much higher at 700 °C, being on the order of ±37.7 °C. For the intensity ratio method, it is found that at lower temperatures, the small anti-Stokes SNR makes accurate thermometry difficult, while at higher temperatures, sensitivity is lost in the calibration. Thus, a trade off is seen between increasing SNR of the anti-Stokes peak through increasing temperature and increasing the uncertainty in the calibration. In general, increased scan times and averaging over multiple measurements can reduce measurement uncertainty by a factor of $N^{-1/2}$ where $N =$ number of measurements. For our experiments, the intensity ratio method was not utilized above 500 °C due to the large errors associated with it.

TABLE I
Uncertainty Estimations of Calibrations for a Single Measurement

Temperature Range (°C)	Stokes Peak Location Calibration Error (°C)	Intensity Ratio Calibration Error (°C)
22-200	±2.12	±8.5
200-500	±3.7	±22
500-700	±5.4	±37.7
700-1000	±7.6	±110

B. Heated AFM Cantilever

The maximum operating voltage for measuring the AFM cantilevers was determined to be 15.5 V (across both cantilever and sense resistor). As can be seen in Fig. 8, the resistance increases with voltage input, until 15.5 V, where the cantilever experiences thermal runaway, and its resistance begins to drop. These resistances were recorded as the Raman laser was incident upon the cantilever. This is important to account for, because the laser produces photoelectrons in the silicon lattice, causing a small increase in circuit current.

The AFM cantilevers were able to reach a maximum temperature near 650 °C, as measured in the center of the heater region by the Stokes method, with an input power of 4.8 mW. A comparison with the anti-Stokes/Stokes ratio method resulted in verification of the data for temperatures at the center of the

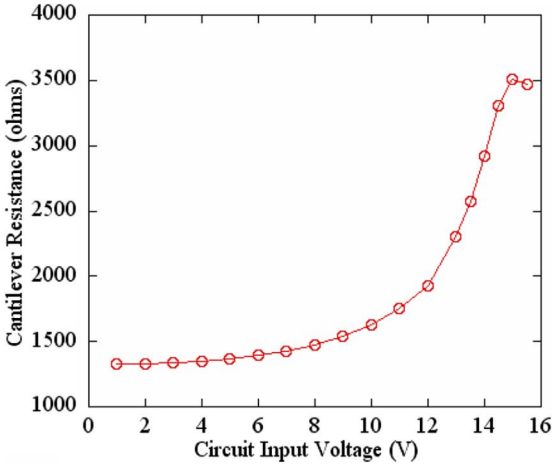

Fig. 8. Calibration of the electrical resistance versus voltage response of the AFM cantilever. Data show a peak resistance occurs near 15 V after which the resistance decreases with an increasing potential difference. All measurements were kept below this voltage to avoid thermal runaway.

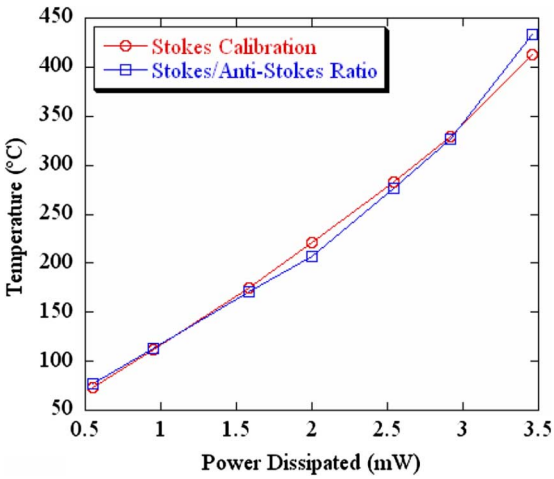

Fig. 9. Comparison of the Stokes shift temperature measurement and the Stokes/anti-Stokes intensity ratio technique. Data show close agreement between the two methods indicating thermal stresses have little effect on Stokes shift measurement accuracy.

heater (Fig. 9). This was the only point monitored with the ratio calibration due to its functional importance. The difference between the two techniques never exceeds 10% over the entire test regime with a maximum difference of 21 °C at 3.45 mW. For all monitored power dissipation, the two calibrations agree within the uncertainties of Table I.

Assuming the deviation between the Stokes shift method and the intensity ratio method is a function of stress, the magnitude of the induced stress may be calculated. Following this assumption, the temperature given by the intensity ratio calibration (being independent of stress) is converted to an equivalent Stokes shift using the linear calibration coefficient ($-0.0232\ \mathrm{cm}^{-1}/°\mathrm{C}$). In essence, if stress is not present, the calculated Stokes shift and the measured shift would be the same. Thus, the difference in the calculated shift and the measured Stokes shift can be used to determine the level of stress in the material using the linear stress coefficient ($-2.859\ \mathrm{cm}^{-1}/\mathrm{GPa}$) determined from four point bend test calibrations [30]. If the calculated shift from the intensity ratio method is lower than

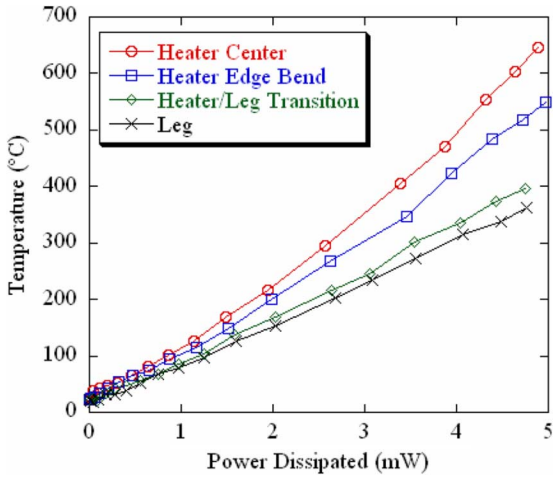

Fig. 10. Measured temperature response of the AFM cantilever as a function of temperature using the Stokes shift method. The four curves correspond to four points between the center of the heater region and the cantilever leg as shown in Fig. 4.

the measured Stokes shift, then the sample is in a state of compressive stress; a tensile stress would be true for the opposite case.

As can be seen in Fig. 9, the data show that heating in the temperature range of 50–425 °C yields the similar temperatures. This shows clearly that stress minimally affects the device measurements, and the Stokes linear temperature coefficient can be used for accurate temperature quantification on this device. Because of the uncertainty of the ratio method at elevated temperatures, the Stokes shift method is the more suitable for extension to high temperature silicon devices. For subsequent measurements on cantilever performance, only the Stokes shift monitor was performed.

The temperature at the four probed points, found using the Stokes linear temperature coefficient, can be seen in Fig. 10 as a function of dissipated power. Intuitively, the center point reaches the highest temperature, while points further away reach lower temperatures as the distance away from the heater is increased. At the peak power dissipation of 4.8 mW, the center of the cantilever reached 650 °C while the point on the cantilever leg farthest from the center was only 375 °C. This indicates that large temperature differences can be expected to exist in the thermal AFM cantilevers which are designed to localize heating to the near tip region.

C. Heated Microbeams

In contrast to the AFM cantilevers, the microbeam measurements were expected to show a wider range of thermal stresses due to their mechanical constraints. Fig. 11 shows that the sample 1A (attached to the oxide layer) was able to reach a maximum temperature on the order of 450 °C with an input power of 275 mW as determined by the Stokes shift method. A comparison with the anti-Stokes/Stokes temperature ratio, however, indicates that stress may be affecting the temperature measurements most notably at higher input powers where the measurements deviate. However, the deviation between the two techniques never exceeds 10% over the entire test regime with a maximum difference of 40 °C at 275 mW. Based on the

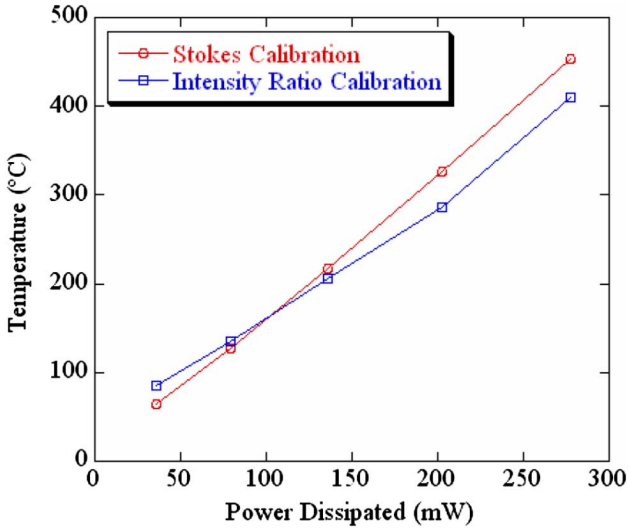

Fig. 11. Comparison of the Stokes shift temperature measurement with the intensity ratio technique for the microbeam on oxide samples (sample 1A). Data show a maximum difference between the two measurement temperatures on the order of 10% indicating that thermal stresses may affect the Stokes shift measurement accuracy.

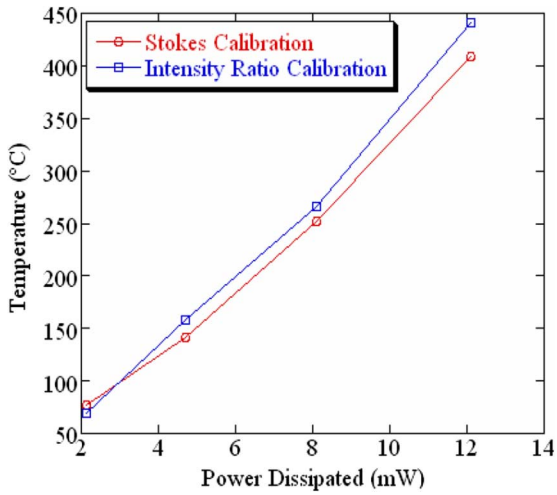

Fig. 12. Comparison of the Stokes shift temperature measurement with the intensity ratio technique for the released microbeam sample (sample 1B). Data show that a maximum difference between the two measurement temperatures on the order of 8%. The smaller difference between the two techniques indicates that a reduction in deformation constraint may increase the accuracy of the Stokes shift method.

differences in the two measurements techniques, it is apparent the heating induces an axial tensile stress on the structure. This increase in tensile stress suggests that the beam is buckling upward out of plane. Due to the fabrication of the sample, the oxide layer places the silicon substrate in residual tension. This causes the wafer to bow and flex the thin-films on the upper surface of the wafer as confirmed by wafer curvature measurements. This curvature places the top portion of the polysilicon layer in residual tension. Because the Raman system is operating at 488 nm, laser depth of penetration is only 700 nm, well above the neutral axis of the entire structure. Thus, tensile residual stresses are found in the polysilicon. As the beam heats, additional flexure of the sample is induced, causing an increase in the tensile stresses due to bending. As

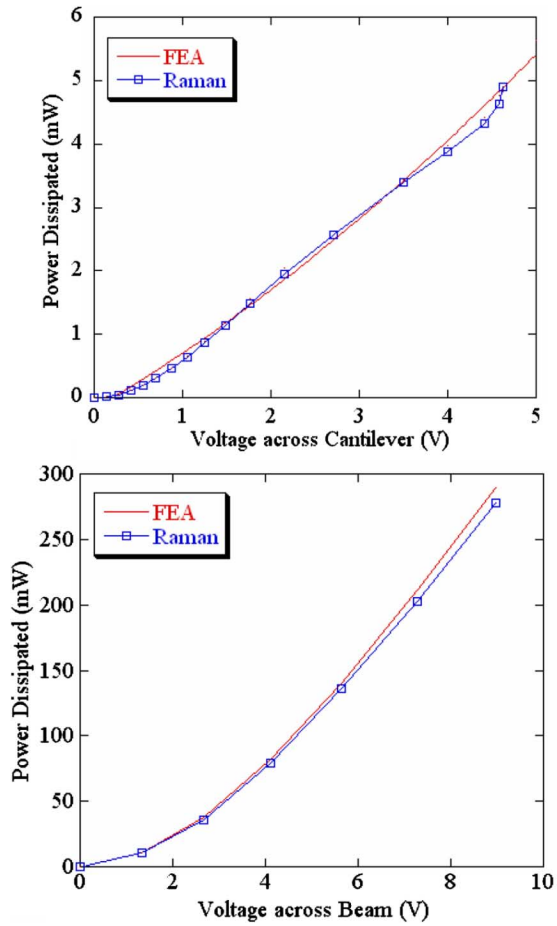

Fig. 13. Comparison of electrical response between experiments and FEA model for the AFM cantilever (top) and microbeam on oxide (sample 1A, bottom). Data show excellent agreement between the predicted values and experiments, being within 5% at all values.

the sample continues to heat it is expected that the rate at which the stress increases will change due to the heating and thermal expansion of the oxide layer underneath the polysilicon layer. Thus, the two measurement techniques are not always expected to diverge. The effects of the change in these constraints for multilayer thermal MEMS devices are difficult to model due to uncertainty in high temperature mechanical properties. However, additional investigation of this effect is warranted.

In the case of the released microbeam, an input power of only 12 mW was needed to reach 450 °C as shown in Fig. 12. The comparison of the intensity ratio technique with the Stokes shift method suggests that the stresses in the structure are smaller. This is consistent with the reduction in displacement constraints on this device. Over the entire measurement range, the maximum deviation between the two techniques was seen to be approximately 8% at the highest input powers.

D. Comparison to FEA Results

For the multi-physics FEA, it was found that both the electrical and thermal behavior must be modeled in order to provide accurate predictions of device behavior. To do this, the voltage placed across the samples was used as an input to the FEA model and the calculated power dissipation was compared to each experimental value. Fig. 13 shows the comparison of the

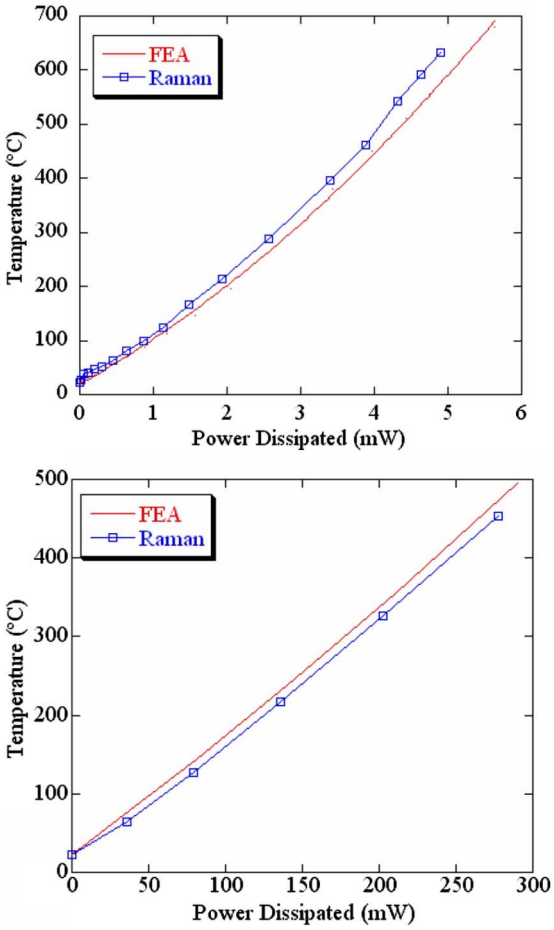

Fig. 14. Comparison of thermal response between Stokes-shift based experiments and FEA model for the AFM cantilever (top) and microbeam on oxide (sample 1A, bottom). Data show excellent agreement between the predicted values and experiments, being within 9% at all values.

model and experimental data which indicate good agreement over the entire range of input voltages for both the AFM cantilever and the microbeam attached to the oxide substrate. Once this result was obtained, the thermal responses of the devices as predicted by ANSYS were compared to the experimental measurements (Fig. 14). Here, only the single-point temperatures in the center of the heater region and the middle of the microbeam were compared. These calculated temperature values are within 9% of the Stokes shift measured values across the entire power range of input powers for both devices. Overall, the modeling shows good agreement with the experimental Stokes temperature measurements without the correction for stress being made. The FEA modeling provides additional evidence that the Stokes shift method may be used as a quick technique for mapping the temperature in some silicon MEMS devices without extensive calibrations. Additional material data and work is needed to model the behavior of stress in these devices with FEA.

IV. Conclusion

This work has shown the ability to use Raman spectroscopy for the measurement of absolute temperature in doped silicon and polysilicon MEMS devices. The method is rather straightforward in calibration without the need of knowing surface optical properties. The Stokes shift method provides adequate temperature accuracy for the measurement of temperature for the device tested in this study even when stress evolution is present. The correction for stress was shown to only provide a change in temperature being less than 10% for all measurements made, decreasing with decreasing mechanical constraints on the devices. This error was seen in the temperature range above 425 °C; however it is apparent that the suspended cantilever geometry of this device carries little or no significant thermal stresses below that temperature. Thus, the Stokes shift method may provide a quick method for screening and mapping the temperature in devices such as this one. High resolution scanning using the anti-Stokes/Stokes intensity ratio may be performed as a validity check, and/or an induced stress prediction to increase the accuracy of the temperature measurement. FEA was used to compare both verify both the electric and thermal response of the heater region of this thermal MEMS device, both at the heater center and across the entire device.

Acknowledgment

The authors wish to thank S. Kearney, L. Phinney, and J. Serrano, Sandia National Laboratories, for their knowledge and discussions of Raman thermometry.

References

[1] E. S. Kolesar, P. B. Allen, J. T. Howard, J. M. Wilken, and N. Boydston, "Thermal-actuated cantilever beam for achieving large in-plane mechanical deflections," *Thin Solid Films*, vol. 355–356, pp. 295–302, 1999.

[2] C. S. Pan and W. Hsu, "An electro-thermally and laterally driven polysilicon microactuator," *J. Micromech. Microeng.*, vol. 7, pp. 7–13, 1997.

[3] D. Bullen, M. Zhang, and C. Liu, "Thermo-mechanical optimization of thermally actuated cantilever arrays," in *Proc. SPIE Int. Soc. Opt. Eng.*, San Diego, CA, 2002, pp. 1–8.

[4] M. Dumitrescu, C. Cobianu, D. Lungu, D. Dascalu, A. Pascu, S. Kolev, and A. v. d. Berg, "Thermal simulation of surface micromachined polysilicon hot plates of low power consumption," *Sens. Act.*, vol. 76, pp. 51–56, 1999.

[5] B. H. Weiller, P. D. Fugua, and J. V. Osborn, "Fabrication, characterization, and thermal failure analysis of a micro hot plate chemical senor substrate," *J. Electrochem. Soc.*, vol. 151, pp. H59–H65, 2004.

[6] V. P. Iordanov, M. Malatek, J. Bastenmeijer, I. T. Young, A. Bossche, G. W. K. V. Dedem, P. M. Sarro, and M. J. Veelekoop, "PCR array on chip-thermal characterization," in *Proc. IEEE Sens.*, Toronto, ON, Canada, 2003, pp. 1045–1048.

[7] E. V. Keuren, M. Cheng, O. Albertini, C. Luo, J. Currie, and M. Paranjape, "Temperature profiles of microheaters using fluorescence microthermal imaging," *Sens. Mater.*, vol. 17, pp. 1–6, 2005.

[8] H. Nagai, Y. Murakami, K. Yokoyama, and E. Tamiya, "High-throughput PCR in silicon based microchamber array," *Biosens. Bioelectron.*, vol. 16, pp. 1015–1019, 2002.

[9] A. H. Epstein, "Millimeter-scale, micro-electro-mechanical systems gas turbine engines," *J. Eng. Gas Turbines Power*, vol. 126, pp. 205–226, 2004.

[10] C. Zhang, L. P. Bernal, K. Najafi, and P. D. Washabaugh, *Mechanical and Thermal Design of a Combustion-Based Thermionic Micro Power Generator.* Washington, DC: Amer. Soc. Mech. Eng. Micro-Electromech. Syst. Div. (MEMS), 2003.

[11] W. P. King and K. E. Goodson, "Thermal writing and nanoimaging with a heated atomic force microscope cantilever," *J. Heat Transf.*, vol. 124, p. 597, 2002.

[12] W. P. King, T. W. Kenny, K. E. Goodson, G. L. W. Cross, M. Despont, U. Dürig, H. Rothuizen, G. K. Binnig, and P. Vettiger, "Design of atomic force microscope cantilevers for combined thermomechanical writing and reading in array operation," *J. Microelectromech. Syst.*, vol. 11, pp. 765–774, 2002.

[13] Y. S. Ju and K. E. Goodson, "Short-time-scale thermal mapping of microdevices using a scanning thermoreflectance technique," *J. Heat Transf.*, vol. 120, pp. 306–313, 1998.
[14] B. Li, J. Roger, L. Pottier, and D. Fournier, "Complete thermal characterization of film-on-substrate system by modulated thermoreflectance microscropy and multiparameter fitting," *J. Appl. Phys.*, vol. 86, pp. 5314–5316, 1999.
[15] S. Dilhaire, E. Schaub, W. Claeys, J. Altet, and A. Rubio, "Localisation of heat sources in electronic circuits by microthermal laser probing," *Int. J. Thermal Sci.*, vol. 39, pp. 544–549, 2000.
[16] J. Christofferson, D. Vashaee, A. Shakouri, and P. Melese, "Real time sub-micron thermal imaging using thermoreflectance," in *Proc. Int. Mech. Eng. Congr. Exhibition (IMECE'01)*, New York, 2001, pp. 1–5.
[17] D. Luerssen, J. A. Hudgings, P. M. Mayer, and R. J. Ram, "Nanoscale thermoreflectance with 10 mK temperature resolution using stochastic resonance," in *Proc. Semi-Therm 21*, San Jose, CA, 2005, pp. 1–5.
[18] S. Grauby, S. Dilhaire, S. Jorez, and W. Claeys, "Temperature variation mapping of a microelectromechanical system by thermoreflectance imaging," *Electron Device Lett.*, vol. 26, pp. 78–80, 2005.
[19] Z. M. Zhang, "Surface temperature measurements using optical techniques," *Annu. Rev. Heat Transf.*, vol. 11, pp. 351–411, 2000.
[20] J. B. Cui, K. Amtmann, J. Ristein, and L. Ley, "Noncontact temperature measurements of diamond by Raman scattering spectroscopy," *J. Appl. Phys.*, vol. 83, pp. 7929–7933, 1998.
[21] G. Viera, S. Huet, and L. Boufendi, "Crystal size and temperature measurements in nanostructured silicon using Raman spectroscopy," *J. Appl. Phys.*, vol. 90, pp. 4175–4183, 2001.
[22] R. Ostermeir, K. Brunner, G. Abstreiter, and W. Weber, "Temperature distribution in Si-MOSFET's studied by micro Raman spectroscopy," *IEEE Trans. Electron Devices*, vol. 39, no. 4, pp. 858–863, Apr. 1992.
[23] S. Perichon, V. Lysenko, B. Remaki, D. Barbier, and B. Champagnon, "Measurement of porous silicon thermal conductivity by micro-Raman scattering," *J. Appl. Phys.*, vol. 86, pp. 4700–4702, 1999.
[24] H. Brugger and P. W. Epperlein, "Mapping of local temperatures on mirrors of GaAs/AlGaAs laser diode," *Appl. Phys. Lette.*, vol. 56, pp. 1049–1051, 1990.
[25] P. W. Epperlein, G. L. Bona, and P. Roentgen, "Local mirror temperatures of red-emitting (Al)GalnP quantum well laser diodes by Raman scattering and reflectance modulation measurements," *Appl. Phys. Lett.*, vol. 60, pp. 680–682, 1992.
[26] M. Kuball, S. Rajasingam, A. Sarua, M. Uren, T. Martin, B. T. Hughes, K. P. Hilton, and R. Balmer, "Measurement of temperature distribution in multifinger AlGaN/GaN heterostructure field-effect transistors using micro-Raman spectroscopy," *Appl. Phys. Lett.*, vol. 82, pp. 124–126, 2003.
[27] A. Chitnis, J. Sun, V. Mandavilli, R. Pachipulusu, M. G. S. Wu, V. Adivarahan, J. Zhang, M. A. Khan, A. Sarua, and M. Kuball, "Self-heating effects at high pump currents in deep ultraviolet light-emitting diodes at 324 nm," *Appl. Phys. Lett.*, vol. 81, pp. 3491–3493, 2002.
[28] M. Bowden and D. Gardiner, "High resolution Raman shift and bandwidth images of stressed silicon," *Int. J. Vibr. Spectroscopy*, pp. 1–6, 1998.
[29] M. Balkanski, R. F. Wallis, and E. Haro, "Anharmonic effects in light scattering due to optical phonons in silicon," *Phys. Rev. B*, vol. 28, pp. 28–34, 1983.
[30] M. R. Abel, T. L. Wright, E. O. Sunden, S. Graham, W. P. King, and M. J. Lance, "Thermal metrology of silicon microstructures using Raman spectroscopy," in *Proc. Semi-Therm 21*, San Jose, CA, 2005, pp. 235–242.
[31] T. L. Wright, *Fabrication and Testing of Heated Atomic Force Microscope Cantilevers*. Atlanta, GA: Georgia Tech., 2005, pp. 1–111.
[32] B. W. Chui, *Advanced Silicon Micromachined Cantilevers for Atomic Force Microscope Data Storage*. Palo Alto, CA: Stanford Univ., 1998.
[33] F. P. Incopera and D. P. DeWitt, *Introduction to Heat Transfer*, 4th ed. New York: Wiley, 2002.
[34] B. Olson, S. Graham, and K. Chen, "A practical extension of the 3-w method to multilayer structures," *Rev. Sci. Instrum.*, vol. 76, pp. 53901-1–53901-7, 2005.
[35] S. Reggiani, M. Valdinoci, L. Colalongo, M. Rudan, and G. Baccarani, "An analytical, temperature-dependant model for majority-and minority-carrier mobility in silicon devices," *VLSI Design*, vol. 10, pp. 467–483, 2000.
[36] Z. Guo, Z. Li, and X. Luo, "Size effect on free convection in a square cavity," in *Proc. Int. Symp. Micro/Nanoscale Energy Conv. Transport*, Antalya, Turkey, 2002, pp. 1–3.
[37] S. P. Kearney, L. M. Phinney, and M. S. Baker, "Spatially resolved temperature mapping of electro-thermal actuators by surface Raman scattering," *J. Microelectromech. Syst.*, vol. 15, no. 2, pp. 314–321, Apr. 2006.

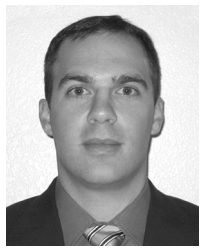

Mark R. Abel received the B.S. degree in mechanical engineering from the University of Missouri, Columbia, in 2002 and the M.S. degree from the Georgia Institute of Technology, Atlanta, in 2005.

He is currently a Process Engineer for Intel Assembly Technology Development, Chandler, AZ.

Tanya L. Wright received the B.S. degree from Iowa State University, Ames, in 2002 and the M.S. degree from the Georgia Institute of Technology, Atlanta, in 2005.

She is currently with Schlumberger Riboud Product Center, Clamart, France.

William P. King received the B.S. degree from the University of Dayton, Dayton, OH, in 1996, and the M.S. and Ph.D. degrees from Stanford University, Stanford, CA, in 1998 and 2002, respectively, all in mechanical engineering.

From 1999 to 2001, he spent 1.5 years working IBM Zurich Research Laboratory, Zurich, Switzerland, on millipede thermomechanical data storage. Since 2002, he has been Assistant Professor in the Woodruff School of Mechanical Engineering, Georgia Institute of Technology, Atlanta.

Dr. King received the CAREER Award from the National Science Foundaiton (NSF) in 2003, the Presidential Early Career Award for Scientists and Engineers (PECASE) from the Department of Energy (DOE) in 2005, and the SME Young Manufacturing Engineer Award in 2006.

Samuel Graham received the B.S. degree from Florida State University, Tallahassee, in 1993 and the M.S. and Ph.D. degrees from the Georgia Institute of Technology, Atlanta, in 1995 and 1999, respectively.

He is an Assistant Professor in the Woodruff School of Mechanical Engineering, Georgia Institute of Technology. From 1999 to 2003, he was a Senior Member of Technical Staff at Sandia National Laboratories, Livermore, CA, where he worked in the Microsystems and Experimental Mechanics Group. His current research is in the area of thermal transport properties of thin films, thermal characterization in MEMS, microscale and nanoscale heat transfer in wide bandgap semiconductors, and processing methods for organic semiconductors devices.

Dr. Graham received the National Science Foundation CAREER Award in 2005 and the Society of Manufacturing Engineers M. Eugene Merchant Outstanding Young Manufacturing Engineer Award in 2004. He is a member of ASME.